Lawrence Berkeley National Laboratory
LBL Publications

Title
Multi-node CdS hetero-nanowires grown with defect-rich oxygen-doped MoS2 ultrathin nanosheets for efficient visible-light photocatalytic H2 evolution

Permalink
https://escholarship.org/uc/item/5mw1z2nt

Journal
Nano Research, 10(4)

ISSN
1998-0124

Authors
Lin, Haifeng
Li, Yanyan
Li, Haoyi
et al.

Publication Date
2017-04-01

DOI
10.1007/s12274-017-1497-3

Peer reviewed

Research Article

Multi-node CdS hetero-nanowires grown with defect-rich oxygen-doped MoS$_2$ ultrathin nanosheets for efficient visible-light photocatalytic H$_2$ evolution

Haifeng Lin[1], Yanyan Li[2], Haoyi Li[1], and Xun Wang[1] (✉)

[1] *Key Lab of Organic Optoelectronics and Molecular Engineering, Department of Chemistry, Tsinghua University, Beijing 100084, China*
[2] *Key Laboratory of Optoelectronic Materials Chemistry and Physics, Fujian Institute of Research on the Structure of Matter, Chinese Academy of Sciences, Fuzhou 350002, China*

ABSTRACT

Developing low-cost and high-efficiency photocatalysts for hydrogen production from solar water splitting is intriguing but challenging. In this study, unique one-dimensional (1D) multi-node MoS$_2$/CdS hetero-nanowires (NWs) for efficient visible-light photocatalytic H$_2$ evolution are synthesized via a facile hydrothermal method. Flower-like sheaths are assembled from numerous defect-rich O-incorporated {0001} MoS$_2$ ultrathin nanosheets (NSs), and {11$\bar{2}$0}-facet surrounded CdS NW stems are grown preferentially along the *c*-axis. Interestingly, the defects in the MoS$_2$ NSs provide additional active S atoms on the exposed edge sites, and the incorporation of O reduces the energy barrier for H$_2$ evolution and increases the electric conductivity of the MoS$_2$ NSs. Moreover, the recombination of photoinduced charge carriers is significantly inhibited by the heterojunction formed between the MoS$_2$ NSs and CdS NWs. Therefore, in the absence of noble metals as co-catalysts, the 1D MoS$_2$ NS/CdS NW hybrids exhibit an excellent H$_2$-generation rate of 10.85 mmol·g^{-1}·h^{-1} and a quantum yield of 22.0% at λ = 475 nm, which is far better than those of Pt/CdS NWs, pure MoS$_2$ NSs, and CdS NWs as well as their physical mixtures. Our results contribute to the rational construction of highly reactive nanostructures for various catalytic applications.

1   Introduction

Recently, energy shortage has been a significant threat to the sustainable development of humans [1]. To meet the future fuel demands, the production of H$_2$ from water splitting by utilizing sunlight is regarded as a promising solution [2]. Thus, considerable efforts have been directed toward exploring efficient semiconductor photocatalysts for H$_2$ formation. Among the semiconducting materials, CdS is of great interest owing to its effective absorption of sunlight, suitable band-structure alignment, and simple fabrication [3, 4].

Address correspondence to wangxun@mail.tsinghua.edu.cn

Nevertheless, pure CdS is usually not active and stable towards photocatalytic H_2 generation [5]. Recently, noble metals, transition metals, and layered transition-metal dichalcogenides (TMDs, such as MoS_2 and WS_2) [6] have been extensively utilized as co-catalysts [7, 8] for CdS, exhibiting enhanced H_2 formation activities owing to the dramatically reduced recombination of charge carriers [9, 10]. Because of the low-cost, rich-deposit, and unique layered structure of TMDs, integrating CdS with TMDs to form hybrids is an attractive method for improving the capability of photoinduced H_2 production.

In heterogeneous catalysis, it is widely considered that smaller nanoparticles with larger surface areas are more reactive towards catalytic reactions than larger ones. However, in reality, irregular nanoparticles with smaller sizes do not always exhibit better activity in catalysis and other surface structure-sensitive reactions [11–13]. The architecture and active sites on specific facets of nanomaterials play a critical role in obtaining outstanding properties. Currently, the design and morphology-controlled synthesis of nanostructures with well-defined reactive crystal planes has become one of the most popular research topics [14–20]. The unsaturated S atoms on the exposed edges of MoS_2 nanosheets (NSs) are the active sites for H_2 generation [21–23]. The under-coordinated S and Cd atoms on the lateral facets of CdS nanowires (NWs) can also be catalytic active sites. Additionally, compared with zero-dimensional nanoparticles, owing to the quantum confinement in the longitudinal and transverse directions of NSs and NWs, respectively, electrons can be transferred selectively along the two-dimensional and one-dimensional (1D) space, which favors the separation of electron–hole pairs, promoting the photo-catalytic reactions.

For most of the reported MoS_2/CdS systems, the products were CdS nanoparticles coated with MoS_2 layers [24, 25], in which the amount of active edge S atoms of MoS_2 layers and the surface reactive S and Cd atoms of CdS nanoparticles were decreased with calcination treatment. Moreover, the granular CdS component is unfavorable for the directional transfer of charge carriers [26]. In this study, novel 1D segmented-flower MoS₂/CdS hetero-NWs were prepared under hydrothermal conditions. The flowers comprised numerous defect-abundant O-incorporated MoS_2 {0001} ultrathin NSs, and the backbones of the CdS NWs were exposed predominantly by {11$\bar{2}$0}. Importantly, the defects introduced into the MoS_2 NSs provided additional active S edge sites for H_2 evolution. A lower energy barrier for H_2 generation and a higher electric conductivity were achieved by incorporating the MoS_2 NSs with O [27]. Furthermore, an intimate heterojunction was formed between the MoS_2 and CdS, which promoted the fast separation and transfer of photogenerated electrons and holes. Benefiting from the above advantages, the 1D multi-node hetero-NWs exhibited excellent activity for photocatalytic H_2 evolution compared with Pt/CdS NWs, pure MoS_2 NSs, and CdS NWs, as well as their physical mixtures.

2 Experimental

All the chemicals were of analytic grade and purchased from SCRC, Shanghai Co., Ltd. They were used for the sample preparation without further purification.

2.1 Synthesis of CdS NWs

In a routine preparation, 0.08 g of $Cd(Ac)_2 \cdot 2H_2O$ and 0.016 g of S powder were dispersed into 9 mL of ethylenediamine under agitation. After stirring for ~45 min, a light yellow suspension was formed, which was then transferred into a 10-mL autoclave and kept at 200 °C for 5 h. Finally, the yellow product was washed with ethanol by centrifugation three times and dried under vacuum conditions.

2.2 Synthesis of MoS_2 NSs

The MoS_2 NSs were synthesized by a previously reported method with some modifications [28]. In a typical procedure, 0.03 g of $Na_2MoO_4 \cdot 2H_2O$ and 0.06 g of thioacetamide were dissolved in 20 mL of water with ~20 min of agitation. Subsequently, the solution was put into a 40-mL autoclave and heated at 200 °C for 24 h. After the reaction, the black product was rinsed with ethanol by centrifugation three times before being dried in a vacuum oven.

2.3 Synthesis of MoS_2 NS/CdS NW hybrids

A specified amount of prepared CdS NWs was added

to 20 mL of water under ultrasonication. The suspension was further sonicated for ~5 min before it was moved to an agitator. Next, 0.04 g glucose was dissolved in the suspension with 2 min of agitation, and then 0.03 g of $Na_2MoO_4 \cdot 2H_2O$ and 0.06 g of thioacetamide were added to the suspension. The mixture was stirred for 20 min. Subsequently, the suspension was transferred into a 40-mL autoclave and kept at 200 °C for 24 h. The product was cleaned with ethanol by centrifugation three times and dried in the vacuum oven. It was denoted as MCx (x = 0.05, 0.10, 0.15, 0.20, 0.25, 0.30, or 0.35), where x represents the quantity (in grams) of CdS NWs used. For comparison, an experiment was performed without using glucose.

2.4 Characterizations

The crystal phases of the products were detected via X-ray diffraction (XRD) analysis using a Bruker D8 Advance X-ray diffractometer employing Cu Kα radiation (λ = 1.5418 Å). X-ray photoelectron spectroscopy (XPS) was performed using a Thermo Fisher ESCALAB 250 Xi spectrometer with monochromatic Al Kα X-ray sources (1,486.6 eV) at 2.0 kV and 20 mA. Raman signals were collected using a LabRAM HR Evolution Raman spectrometer. Ultraviolet–visible (UV–vis) absorption spectra were recorded using a Shimadzu UV 3600 spectrometer. Transmission electron microscopy (TEM), high-resolution TEM (HRTEM), dark-field scanning transmission electron microscopy (STEM), and energy-dispersive X-ray spectroscopy (EDX) element mapping were performed using an FEI Tecnai G2 F20 S-Twin microscope operated at 200 kV. Scanning electron microscopy (SEM) was performed using a Hitachi S5500 Field Emission Gun Scanning Electron Microscope at 5 kV. The Brunauer–Emmett–Teller (BET) specific surface areas and pore-size distributions were measured using a Micromeritics Tristar 3020 II automatic adsorption instrument. Inductively coupled plasma (ICP) emission spectroscopy was performed using 2RIS Intrepid II XSP ICP-OES equipment. Thermogravimetric analysis (TGA) and differential thermal analysis (DTA) were performed using a NETZSCH STA 449F3 analyzer with Ar as the protection gas. The electron paramagnetic resonance (EPR) signals were obtained at 113 K using a JEOL FA-200 spectrometer. The photoluminescence (PL) spectra were obtained using a Varian Cary Eclipse Fluorescence spectrophotometer under excitation by laser light at λ = 400 nm.

2.5 Photoelectrochemical performance

Photoelectrochemical water reduction was conducted for photocathodes of CdS NWs, MoS_2 NSs, and MoS_2/CdS composites using a three-electrode CHI 650D electrochemical workstation. The counter electrode was a Pt sheet, and the reference electrode was a saturated calomel electrode (SCE). For the preparation of the working electrode, the catalyst suspension (200 μL, 5 g·L^{-1} in ethanol) was dropped onto the F-doped s glass (2 cm × 2 cm) surface, forming a film after drying naturally for 24 h, and then the catalyst-decorated working electrodes were calcined at 450 °C for 1 h to counter the peeling of the catalyst that occurred during the measurement. An aqueous solution containing 0.5 M Na_2S and 0.5 M Na_2SO_3 was used as the electrolyte. The photoelectrochemical activity was measured using the linear-sweep voltammetry method with a scanning rate of 10 mV·s^{-1} and a bias potential of 0.01 mV. A 300-W Xe lamp equipped with a 400-nm cutoff filter was employed for the irradiation, and a shutter was used to modulate the light and dark conditions during the test.

2.6 Electrochemical measurements

Galvanostatic electrochemical impedance spectroscopy (EIS) was performed using a Princeton workstation with the same three-electrode setup that was used for the photoelectrochemical water reduction, with a 0.5 M Na_2SO_4 aqueous solution as the electrolyte. The amplitude and frequency range were 0.1 mA and 0.1–10^5 Hz, respectively. A bias current of 0.3 mA was utilized for the test.

The Mott–Schottky curves were also examined using the Princeton workstation employing the same three-electrode configuration that was used for the photoelectrochemical water reduction with the 0.5 M Na_2SO_4 aqueous electrolyte. Here, the amplitude and frequency were 0.01 V and 1 kHz, respectively.

2.7 Photocatalytic property of H_2 evolution

The photocatalytic H_2-generation activities of CdS

NWs, MoS$_2$ NSs, Pt/CdS NWs, a physical mixture of MoS$_2$ NSs and CdS NWs, and MoS$_2$/CdS hybrids were measured with visible-light irradiation. Before each test, 0.1 g of the catalyst was dispersed in 100 mL of a lactic-acid aqueous solution (10 vol.%) after ultrasonication for ~5 min. To determine the effect of the lactic-acid concentration on the H$_2$ formation, the volume of lactic acid was changed to 10, 20, 30, 50, and 70 mL. The reactions were conducted using a photocatalytic H$_2$ evolution system furnished by PerfectLight, Beijing Co., Ltd. The visible-light source was a 300-W Xe lamp equipped with a 400-nm cutoff filter. To determine the quantum yields of photocatalytic H$_2$ generation with different irradiation wavelengths, bandpass filters of 420, 450, 475, 500, and 520 nm were used for the reaction. The testing temperature was maintained at 5 °C using a homeothermic cooling circulation pump. A gas chromatograph containing a thermal-conductivity detector was used to detect online the formation of H$_2$ every hour.

The quantum yield was calculated using the following equation [29]

$$
\begin{aligned}
&\text{Quantum yield} \\
&= \frac{\text{Number of reacted electrons}}{\text{Number of incident photons}} \times 100\% \\
&= \frac{2 \times \text{ number of formed H}_2 \text{ molecules}}{\text{Number of incident photons}} \times 100\% \\
&= \frac{2 \times N_{\text{H}_2}}{N_{\text{i}}} \times 100\% \\
&= \frac{2 \times N_{\text{H}_2}}{\dfrac{I \times A \times t \times \lambda}{h \times c}} \times 100\%
\end{aligned}
$$

Here, N is the number of electrons, photons, or molecules; I is the light intensity; $A = 24.6$ cm^2 ($r = 2.8$ cm) is the irradiation area; $t = 3{,}600$ s is the irradiation time; λ is the wavelength of incident light (nm); $h = 6.63 \times 10^{-34}$ J·s is the Planck constant; and $c = 3.0 \times 10^8$ m·s^{-1} is the speed of light.

3   Results and discussion

3.1   Morphology and structural characterizations of MoS$_2$/CdS heterostructures (HRSs)

The CdS NWs were prepared using an ethylenediamine-assisted solvothermal method, and the MoS$_2$ NSs were obtained under hydrothermal conditions. For the construction of MoS$_2$ NS/CdS NW composites (denoted as MCx, where x = 0.05, 0.10, 0.15, 0.20, 0.25, 0.30, or 0.35 and is the input amount (grams) of CdS NWs), MoS$_2$ NSs were grown on the surface of CdS NWs via the hydrothermal method. The XRD patterns for the MoS$_2$ NSs, CdS NWs, and their hybrids are shown in Fig. 1(a). The signals corresponding to CdS are evident for all the composites; however, the MoS$_2$ signal is only observed at higher loading percentages, such as MC0.05 and MC0.10, possibly because of the small amount and weak crystallinity (broadened diffraction peaks) of the MoS$_2$ NSs in the HRSs. For the individual CdS NWs and their hybrids, all the diffraction peaks of CdS can be assigned to the wurtzite structure (JCPDS card No. 80-0006). Interestingly, compared with the pristine 2H-MoS$_2$ phase (JCPDS card No. 75-1539), the (002) diffraction peak of the synthesized MoS$_2$ NSs was significantly shifted from ~14° to a position lower than 10°, indicating the formation of a new lamellar structure [27] with enlarged interlayer spacing (d spacing increased from 6.26 to 9.50 Å). In accordance with the XRD results, the Raman signals shown in Fig. 1(b) confirm the phase purity of the CdS NWs (1LO 302 cm^{-1}) [30, 31] and MoS$_2$ NSs (E$^1_{2g}$ 380 cm^{-1}, A$_{1g}$ 404 cm^{-1}) [32, 33] in the individual products and their composites. Mo–O bond vibrations (B$_{2g}$ 282 cm^{-1}, B$_{1g}$ 337 cm^{-1}) [27, 34] were identified in both the MoS$_2$ NSs and the MoS$_2$/CdS HRSs (e.g., MC0.05), suggesting the incorporation of O in the MoS$_2$ crystal structure. As previously reported [27], MoS$_2$ ultrathin NSs with an increased interlamellar spacing are accompanied by O incorporation (existing as Mo–O bonds). In contrast to the MoS$_2$ NSs prepared by Zhou W. [28] and Weng B. [35], our MoS$_2$ NSs exhibited a dramatic shift of the (002) XRD diffraction to a lower angle, which shows that the layer spacing of our MoS$_2$ NSs was far larger than those of the former two. Weng et al. [35] employed a reaction volume of 50 mL, which is larger than the volume of 40 mL used in our synthesis. Interestingly, when the reaction temperature was increased from 200 to 220 °C, the (002) XRD peak of the MoS$_2$ NSs product (Figs. S1 and S2 in the Electronic Supplementary Material (ESM)) moved to the same position
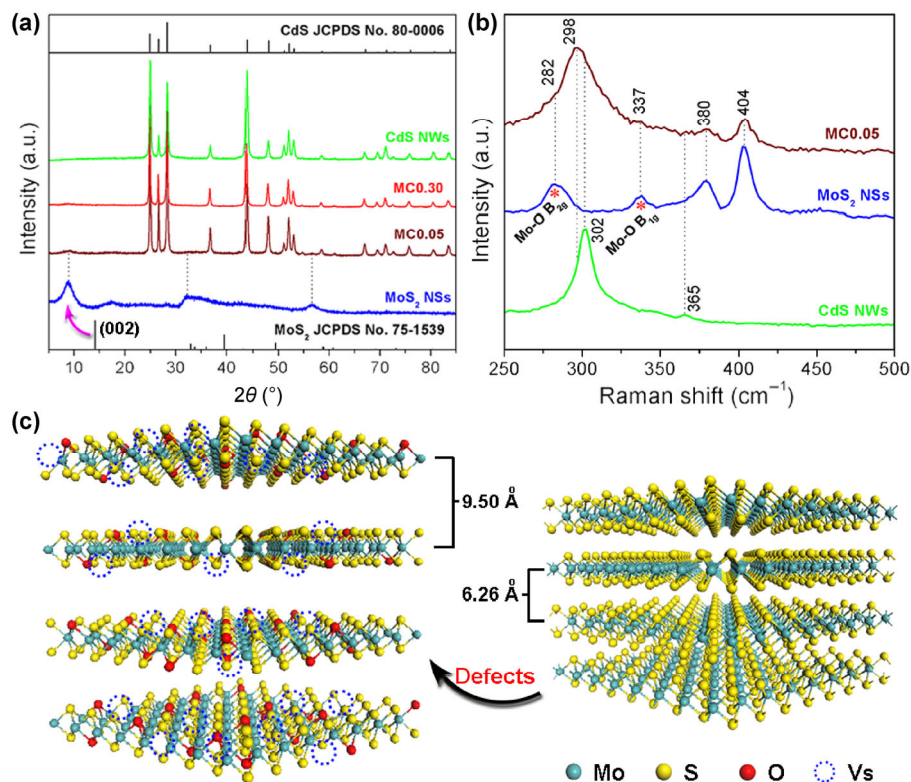
Figure 1 (a) XRD patterns for MoS$_2$ NSs, CdS NWs, and hybrids of MC0.05 and MC0.30. (b) Raman spectra for MoS$_2$ NSs, CdS NWs, and MC0.05. (c) Atomic modes showing the enlargement of the interlayer spacing when the O and S vacancies were incorporated in the MoS$_2$ structure.

as that of the reference JCPDS card (No. 75-1539), indicating that the interlayer spacing of the MoS$_2$ product decreased to the common value of 6.26 Å. Moreover, the Mo–O bonds were absent in the MoS$_2$ NSs fabricated at 220 °C (Fig. S3 in the ESM), which precludes the O doping in this product. Therefore, the O doping in the MoS$_2$ ultrathin NSs could have been due to the lower synthesis temperature and insufficient reaction course, which caused part of the Mo–O bonds from the molybdate precursor to remain in the obtained MoS$_2$ NSs.

To identify the reason for the expansion of the interlayer spacing of our MoS$_2$ NSs, the TGA and DTA curves of the O-incorporated MoS$_2$ NSs were measured in the temperature range of 50 to 600 °C (Fig. S4 in the ESM). We observed little weight loss and no apparent endothermal or exothermal peak. Thus, the notable increase in the layer spacing of our MoS$_2$ NSs is mainly attributed to their specific structure rather than the intercalated molecules. MoS$_2$ is a layered material [36] composed of covalently bonded

S–Mo–S sheets that are bound by weak van der Waals forces. The bond length of Mo–O is smaller than that of Mo–S; thus, the interlamellar spacing of the MoS$_2$ layers could have been increased when a portion of the Mo–S bonds were replaced by Mo–O bonds through the O incorporation, owing to the weakened attraction between the layers. Moreover, there were abundant defects in the ultrathin MoS$_2$ NSs—including Mo^{5+} and S$_2^{2-}$ species (discussed later), S vacancies (as confirmed by the intense and broadened EPR signal at g = 2.07 (Fig. S5 in the ESM)) [37], and numerous additional edges formed by the relatively disordered atomic arrangement on the NS basal plane (elaborated below)—which may have contributed to the increase of MoS$_2$ layer spacing by intensifying the lattice expansion [38, 39]. A schematic of 2H-MoS$_2$ cell models displaying the enlargement of the interlayer spacing with O doping and S vacancies is presented in Fig. 1(c).

TEM images of individual MoS$_2$ NSs and CdS NWs with uniform morphologies are shown in Figs. 2(a) and 2(d), respectively. The MoS$_2$ NSs exhibit a small
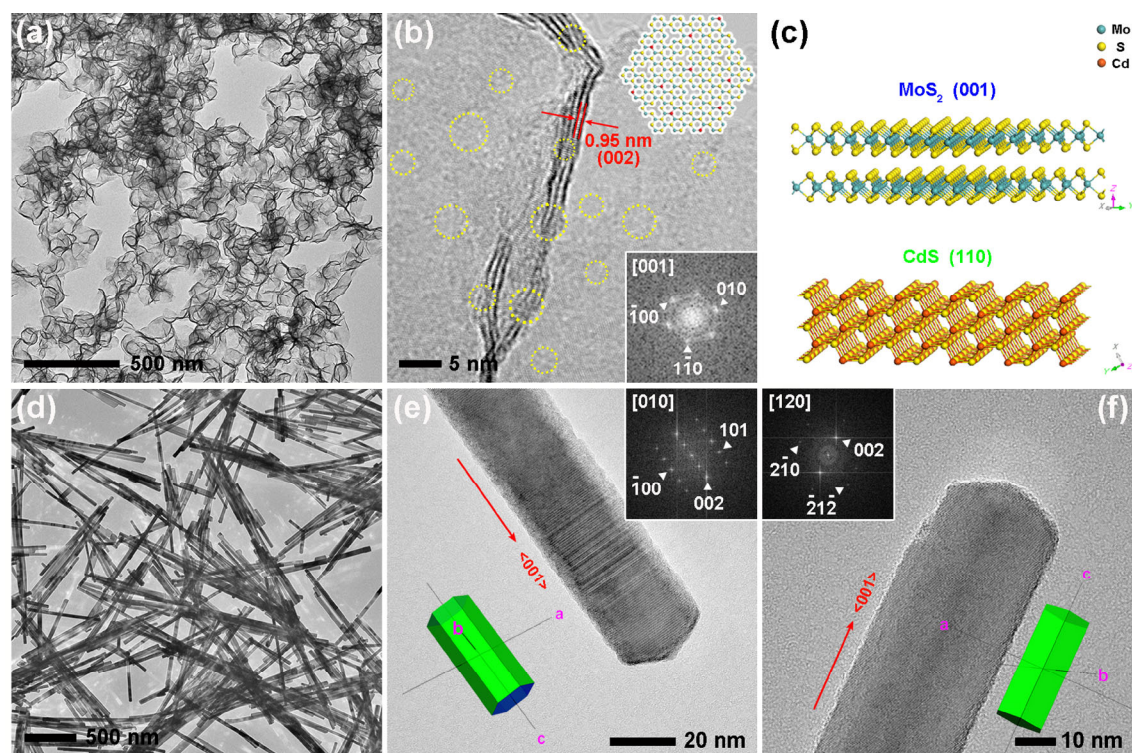
Figure 2 TEM and HRTEM images of ((a) and (b)) MoS_2 NSs and ((d)–(f)) CdS NWs. (c) Atomic structures of MoS_2 {0001} and CdS {11$\bar{2}$0}.

thickness of approximately 3–5 nm and a lateral size of ~200 nm, and the CdS NWs exhibit a major diameter of 20–50 nm and a length of approximately 1–1.5 μm. Figure 2(b) shows an HRTEM graph of the MoS_2 NSs, indicating that rich defects (such as dislocations and distortions, as marked by the yellow dashed circles) were present in both the basal surface and the cross section of the NSs. An enlarged interlayer spacing of 0.95 nm was detected, which corresponds to the (002) crystal plane of 2H-MoS_2. According to the fast Fourier transformation (FFT) analysis for one periodic area of a MoS_2 NS, the lattice fringes were indexed to [001] diffraction. Hence, the basal planes of the NS perpendicular to the [001] zone axis were fixed as {001} (equivalent to {0001} facets). According to the HRTEM and FFT results shown in Fig. 2(e), the top and bottom planes of the CdS NW perpendicular to the [010] zone axis were (2$\bar{1}$0) and ($\bar{2}$10) (equivalent to {11$\bar{2}$0} facets), and the growth of the CdS NW was parallel to <001> (equivalent to <0001>), i.e., along the c-axis. When the CdS NW was in the [120] direction, the lattice fringes terminated sharply at the (2$\bar{1}$0) and ($\bar{2}$10) boundaries,

confirming that these two edges formed the facets of the NW surface. Therefore, the CdS NW was surrounded by six {11$\bar{2}$0} facets and stretched preferentially along the c-axis, whereas the MoS_2 NS was exposed exclusively by {0001} facets. To clarify the related orientations, simulated models are shown in the insets for the corresponding samples. The atomic structures of MoS_2 {0001} and CdS {11$\bar{2}$0} are illustrated in Fig. 2(c). For comparison, the structures of CdS {01$\bar{1}$0} and {0001} are shown in Fig. S6 in the ESM.

The morphology evolution of the MoS_2 NS/CdS NW HRSs with varying composite ratios was examined using TEM and SEM. At a large MoS_2 concentration of MC0.05 (Fig. 3(a)), the product exhibited a homogeneous segmented-flower NW architecture, in which the flowers were assembled by numerous intersecting ultrathin NSs. The stereo appearance of the MC0.05 sample was clearly verified by SEM (Fig. 3(d)). When the MoS_2 percentage was reduced to a moderate value, e.g., MC0.15 (Fig. 3(b)), the bigger flowers were scattered into many smaller ones that were distributed uniformly on the NW surface. When the MoS_2 content
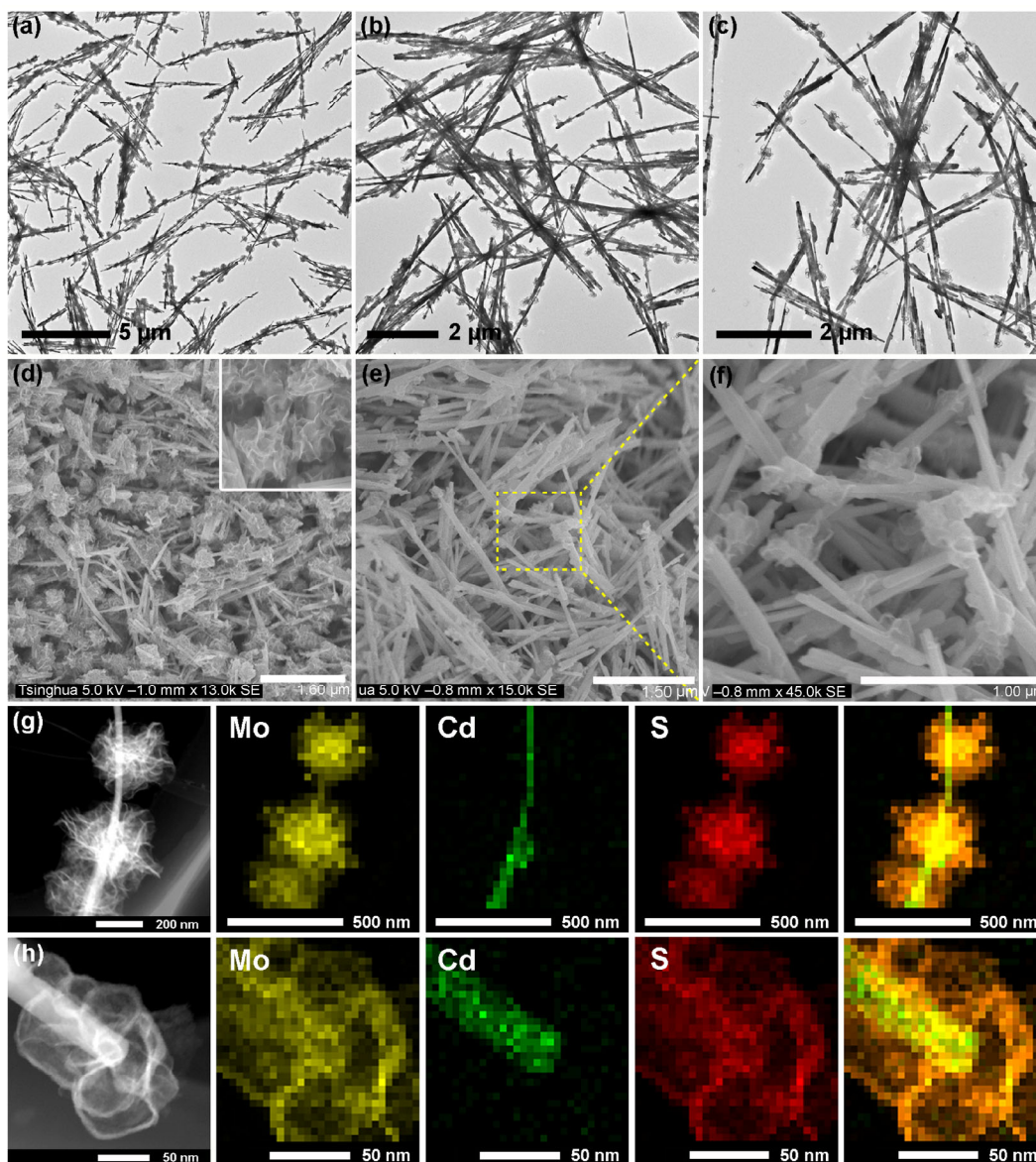
Figure 3 TEM and SEM graphs of the MoS$_2$ NS/CdS NW HRSs ((a) and (d)) MC0.05, (b) MC0.15, and ((c), (e), and (f)) MC0.30. The corresponding STEM and element-mapping results for MC0.05 and MC0.30 are presented in (g) and (h), respectively.

was further reduced, e.g., MC0.30 (Fig. 3(c)), the number of flowers wrapped around the NW was diminished, and the small flowers comprised only several NSs. The morphology of the MC0.30 product was examined by SEM, as shown in Fig. 3(e), which was amplified to obtain Fig. 3(f). The dark-field STEM photographs and corresponding EDX element-mapping results for the MC0.05 and MC0.30 hybrids are shown in Figs. 3(g) and 3(h), respectively. The images clearly show that the ultrathin NSs encircling the NWs were solely composed of MoS$_2$ and that the NWs should

be attributed to the CdS component.

An HRTEM image of MC0.30 is shown in Fig. 4, indicating the layered structure of the NSs and the single-crystalline characteristic of the NWs. Similar to the individual MoS$_2$ NSs (Fig. 2(b)), the MoS$_2$ NS sheath after hybridization exhibited an increased interlayer spacing of 0.95 nm (assigned to the (002) plane) and numerous defects throughout the basal plane and cross section. According to the HRTEM graph and the corresponding FFT analysis of the CdS NW stem, the NW was [010]-oriented and extended
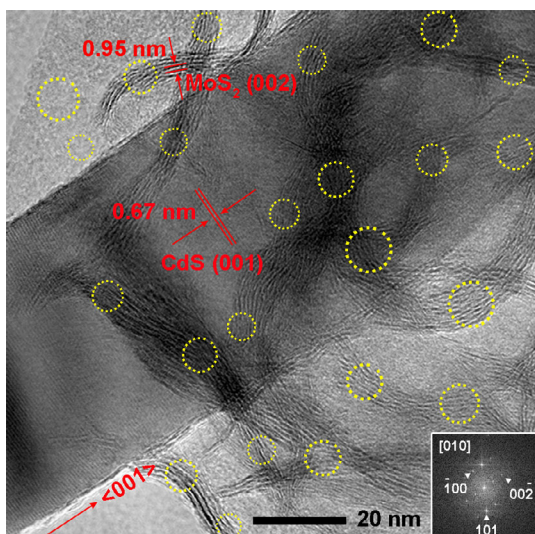
Figure 4 HRTEM photo of the MoS$_2$/CdS composite MC0.30.

Figure 5 TEM graphs of the MoS$_2$/CdS hybrid obtained after reaction for (a) 6, (b) 12, (c) 18, and (d) 24 h. (e) Proposed growth process for the 1D MoS$_2$ NS/CdS NW hybrids.

the crystal lattices preferentially along the <001> axis. In a comparison experiment, the glucose was eliminated from fabrication of MC0.05. The resulting product is shown in Fig. S7 in the ESM. Compared with MC0.05, the product synthesized without glucose exhibited significant nonuniformity: Some NWs were heavily coated by NSs, but the majority of them were merely encircled by a few NSs. Therefore, glucose played an important role in improving the dispersity of the MoS$_2$ NSs grown on the CdS NW surface. To investigate the formation mechanism of our MoS$_2$/CdS multi-node hetero-NWs, the growth processes of MC0.05 were examined. Figure 5 shows that when the reaction was suspended at 6 h (Fig. 5(a)), many tiny scattered particles were generated on the NW surface (indicated by yellow triangles), which could have been the C nanocrystals produced by the decomposition of glucose at the high temperature of 200 °C [40]. When the reaction time was extended to 12 h (Fig. 5(b)), the morphology of the product remained nearly unchanged. After 18 h of the reaction (Fig. 5(c)), small pieces of NSs started to appear on the NWs (indicated by red dashed circles). Finally, after 24 h of the reaction, uniform MoS$_2$/CdS multi-node NWs were formed (Fig. 5(d)). Therefore, because of the lower content of dissolved glucose (0.01 M), the as-formed C component only occupied a small area on the CdS surface (Fig. 5(a)) and had a negligible effect on the intimate contact between the MoS$_2$ and CdS. Because of the smaller size and amount of C species on the NWs, it was difficult to fix the
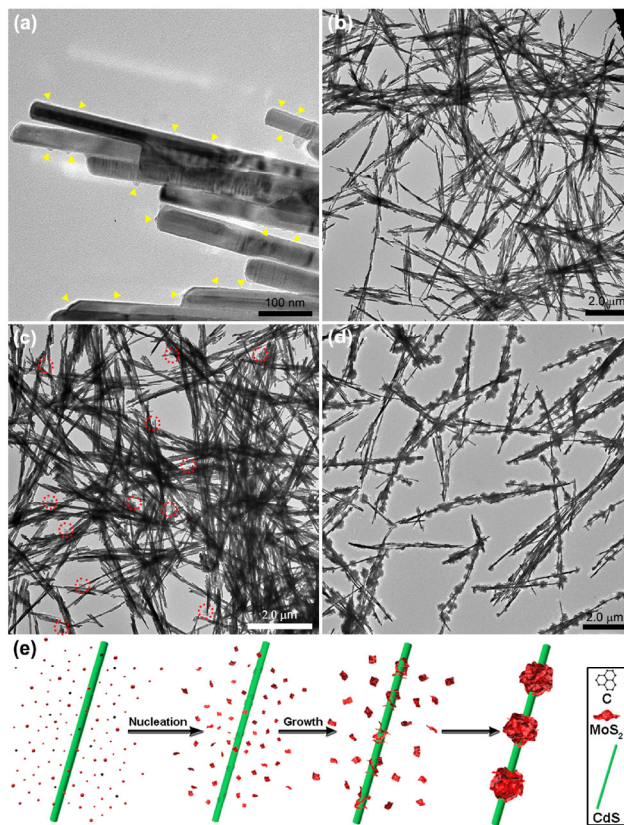
specific composition. According to Ref. [40], the C component might be amorphous and is capable of enhancing the electrical conductivity of the hybrid. Moreover, compared with the glucose-free preparation, the uniformly dispersed C nanocrystals on the CdS NWs could have provided numerous additional nucleation sites, improving the homogeneity of the MoS$_2$ growth. According to the aforementioned results, the formation (Fig. 5(e)) of the multi-node MoS$_2$/CdS hetero-NWs probably occurred as follows. Initially, in the first few hours, the glucose was decomposed into numerous small C nanoparticles [40], which emerged on the pre-existing CdS NWs surface through the heterogeneous nucleation [41, 42] at 200 °C under hydrothermal conditions. Subsequently, the molybdate precursor MoO$_4^{2-}$ slowly transformed into MoS$_2$ seeds by reacting with thioacetamide molecules during the longer reaction courses. Then, after the concentration of the seeds reached a supersaturated point [43, 44], the MoS$_2$ NSs nuclei evolved on the NWs surface via

heterogeneous nucleation and adsorption by C species. Finally, the segmented MoS_2 flowers encircling the NWs were gradually formed via the further growth and assembly of the NSs, which was induced by the Ostwald ripening.

The interaction between the MoS_2 and CdS components in the hybrid MC0.30, as well as the related surface composition and elemental valence states, were investigated using XPS. According to the fitting results, before hybridization, the major Mo $3d_{5/2}$ and $3d_{3/2}$ binding energies in individual MoS_2 NSs were determined as 228.5 and 231.8 eV (Fig. 6(a)), respectively, which are assigned to Mo^{4+} species [45, 46]. The satellite Mo 3d peaks around 229.2 and 233.0 eV are attributed to the Mo^{5+} chemical state [47, 48], which probably originated from the incorporation of O. The presence of the Mo^{5+} component was verified by the EPR signals at g = 1.92, 1.94, and 1.97 (Fig. S5 in the ESM) [48–50]. Regarding the Cd element in the pure CdS NWs, the Cd $3d_{5/2}$ and $3d_{3/2}$ signals located at 405.0 and 411.8 eV (Fig. 6(b)) correspond to the Cd^{2+} state [51]. After the

hybridization of the MoS_2 NSs with CdS NWs, the binding energies of Mo 3d in MC0.30 exhibited an apparent redshift of ~0.3 eV compared with that for individual MoS_2 NSs. In contrast, the Cd 3d peaks in MC0.30 exhibited a blue-shift of ~0.3 eV with respect to that for individual CdS NWs (Fig. 6(b)). Therefore, the electronic density of Mo in MC0.30 was higher than that for pure MoS_2 NSs; however, MC0.30 had a lower electronic density of Cd than individual CdS NWs. These results indicate that the transfer of electrons from CdS to MoS_2 occurred after the two materials were combined [52], which agrees well with the fact that the electronegativity of Mo is higher than that of Cd (in Pauling scale, 2.16 and 1.69 for Mo and Cd, respectively). Consequently, the formation of heterojunctions and Cd–S–Mo bonds at the interfaces was expected. Apart from the Raman vibrations (Fig. 1(b)), the incorporation of O in the MoS_2 NSs both before and after hybridization was confirmed by the presence of the Mo–O bond signal (~235.6 eV) [47] in the Mo 3d spectra (Fig. 6(a)), as well as by the
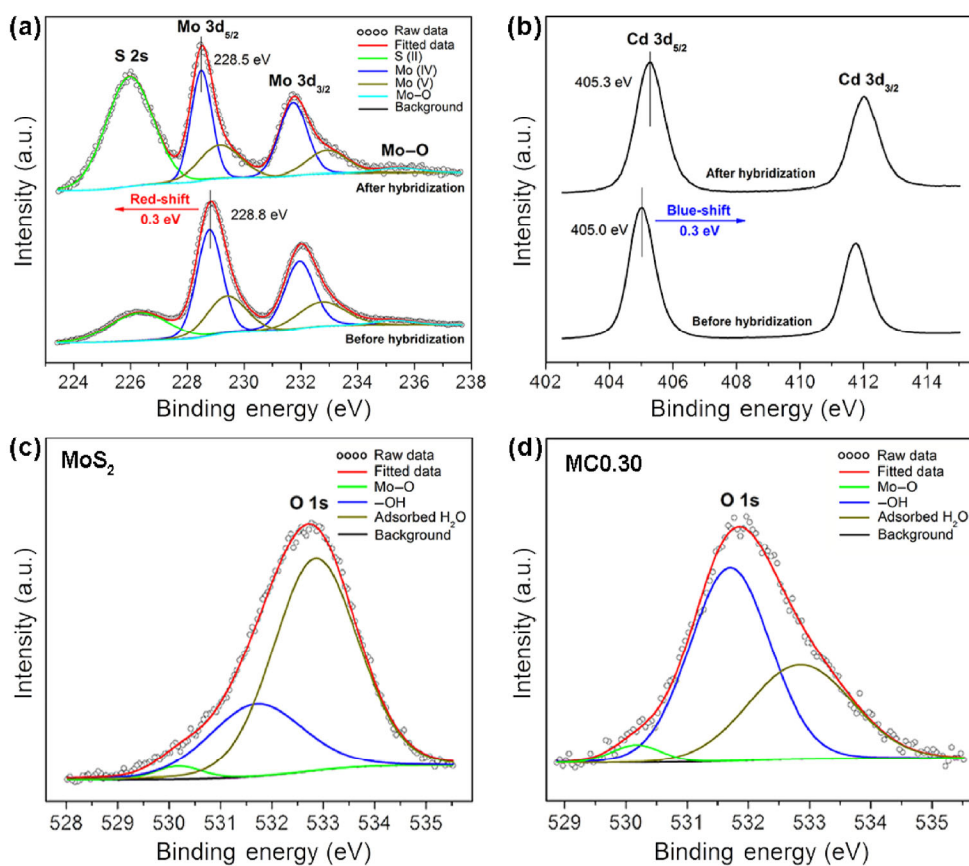

Figure 6 (a) Mo 3d, (b) Cd 3d, and ((c) and (d)) O 1s XPS spectra for MoS_2 NSs, CdS NWs, and the composite MC0.30.

Mo(IV)–O bond peak (~530.1 eV) [53] in the O 1s spectra for both the MoS$_2$ NSs and the MC0.30 HRSs (Figs. 6(c) and 6(d)). These results suggest that O was incorporated in the MoS$_2$ lattices and replaced S at the S sites. In addition, the S 2p spectra for the CdS NWs, MoS$_2$ NSs, and MC 0.30 HRSs, together with the O 1s spectrum for the CdS NWs, were analyzed, as shown in Fig. S8 in the ESM. Interestingly, in contrast to the S^{2-} component, another set of doublets with binding energies around 163.1–164.3 eV was indicated by the S 2p signals for both the MoS$_2$ NSs and the MC0.30 hybrid, suggesting that S$_2^{2-}$ ligands were present in these two samples [48, 54]. Generally, S$_2^{2-}$ species are accompanied by the emergence of Mo^{5+} [47], and both S$_2^{2-}$ and Mo^{5+} can serve as active sites for the H$_2$ evolution reaction [48]. Analysis of the peak area revealed that the Mo^{5+} content in the MoS$_2$ NSs and MC0.30 was approximately 36% and 31%, respectively. The S$_2^{2-}$ content in the MoS$_2$ NSs and MC0.30 was calculated to be approximately 26% and 18%, respectively. In accordance with the EPR analysis

(Fig. 1), the ratio of Mo to S in the MoS$_2$ NSs was determined by ICP to be 1:1.80, indicating the presence of S vacancies. Hence, the defect-rich structure of the MoS$_2$ NSs was recognized from the ICP results and the quantified data for the S$_2^{2-}$ and Mo^{5+} species.

3.2   Photocatalytic properties

In the reaction of photoelectrochemical water reduction, the photocathode of the MoS$_2$ NS/CdS NW HRS MC0.30 exhibited a significantly higher photocurrent density than those of individual MoS$_2$ NSs and CdS NWs (Fig. 7(a)), suggesting that the MC0.03 composite had the best performance for generating and suppressing the recombination of photoinduced charge carriers [29]. Thus, the hybrid MC0.30 is anticipated to exhibit outstanding photocatalytic reactivities. Figure 7(b) shows the averaged H$_2$ formation rate with different photocatalysts under visible-light irradiation ($\lambda >$ 400 nm), where MoS$_2$ NSs, CdS NWs, Pt-loaded (3 wt.% Pt) CdS NWs, and the physical mixture of MoS$_2$ NSs and CdS NWs are all of lower activities.
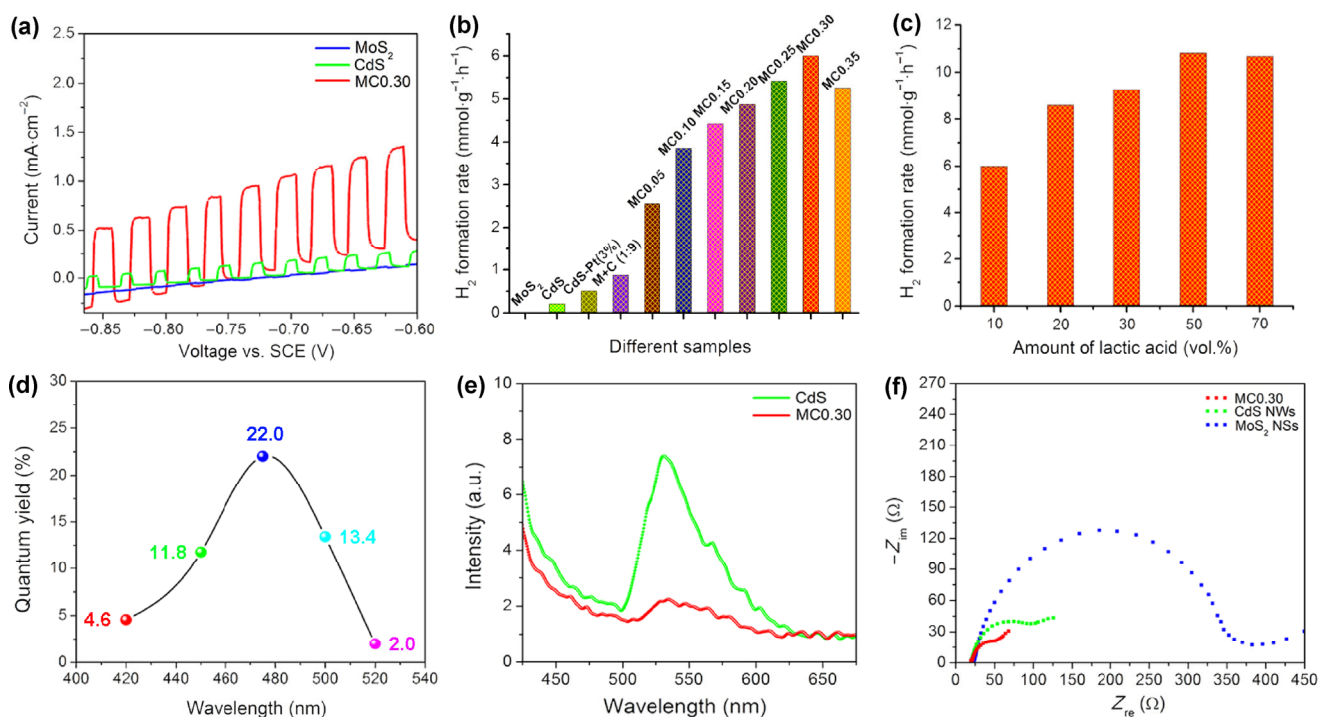

Figure 7   (a) Comparison of the photoelectrochemical performance among MoS$_2$ NSs, CdS NWs, and MC0.30. (b) Averaged H$_2$ evolution rate of MoS$_2$ NSs, CdS NWs, Pt/CdS NWs, a physical mixture of MoS$_2$ NSs and CdS NWs, and 1D MoS$_2$/CdS hybrids with different Mo-to-Cd ratios. (c) H$_2$-generation rates of MC0.30 at varying volume proportions of lactic acid to water. (d) Irradiation wavelength-dependent quantum yield of photocatalytic H$_2$ formation by MC0.30. (e) PL emission spectra and (f) EIS Nyquist plots for MoS$_2$ NSs, CdS NWs, and MC0.30.

Interestingly, the H_2 evolution performance was significantly improved when the 1D MoS_2 NS/CdS NW HRSs (MCx, x = 0.05, 0.10, 0.15, 0.20, 0.25, 0.30, and 0.35) were used as the catalysts, and the highest H_2-generation rate of 6.02 mmol·g^{-1}·h^{-1} (~28 times that of pure CdS NWs) was obtained for MC0.30 (see Fig. S9 in the ESM for details on the H_2 evolution with respect to the irradiation time). Moreover, the average H_2 evolution rate of MC0.30 remained steady during the continuous photocatalytic reaction for 10 h (Fig. S10 in the ESM), indicating that our MoS_2 NS/CdS NW HRSs had good stability for photocatalytic H_2 evolution. The BET specific areas, adsorption isotherms, pore-size distributions, and ICP results for these HRSs are shown in Fig. S11 and Table S1 in the ESM. To determine the effect of the amount of hole scavengers on the H_2-formation activity of MC0.30, different ratios of lactic acid to water were employed for the reaction. The highest rate of 10.85 mmol·g^{-1}·h^{-1} was achieved at a lactic-acid dosage of 50 vol.% (Fig. 7(c)). The H_2 evolution rate in our study is far better than those of most previously reported MoS_2/CdS composite systems (see Table S2 in the ESM) [4, 24, 25, 48, 55]. Moreover, the dependence of the quantum yield of the photocatalytic H_2 evolution of MC0.30 on the irradiation wavelength was examined in detail (Fig. 7(d)). The maximum quantum yield of 22.0% was obtained at λ = 475 nm. The quantum yield of MC0.30 increased from 2.0% to 22.0% when the illumination wavelength was changed from 520 to 475 nm, which is consistent with the enhancement of the light absorption of the photocatalyst (Fig. S12 in the ESM). Nevertheless, when the excitation wavelength was changed from 475 to 420 nm, MC0.30 exhibited a slight increase in light absorption but a decrease in quantum yield. A careful comparison between the absorption spectra of MoS_2 NSs and CdS NWs indicates that in the wavelength range of 475 to 420 nm, the light absorption slightly increased for the CdS NWs, whereas the absorption capability of the MoS_2 NSs decreased. Therefore, the decline in the quantum yield of MC0.30 in the wavelength range of 475 to 420 nm is mainly attributed to the reduced light harvest from the grown MoS_2 NS component. To identify the origin of the activity improvement, the PL spectra for MC0.30 HRSs, pure MoS_2 NSs, and pure CdS NWs were compared

(Fig. 7(e)). The HRSs exhibited a far lower PL intensity than the CdS NWs, suggesting that they had a better separation efficiency for photogenerated electrons and holes [56]. This agrees well with the photocurrent-response analyses. The PL signal for the MoS_2 NSs was negligible (not shown), which could be related to its luminescence-inactive multilayer structure [36, 57]. The electrochemical impedance spectra for the MC0.30 HRSs and individual MoS_2 NSs and CdS NWs are shown in Fig. 7(f). The arc radius of the Nyquist curve is substantially smaller for MC0.30 than for the pure MoS_2 NSs and CdS NWs, indicating that the composite had a significantly lower charge-transfer resistance than the two single components [58–60]. Accordingly, owing to the higher conductivity of MC0.30 compared with the MoS_2 NSs and CdS NWs, the capability of MC0.30 for photoelectrochemical water reduction was enhanced, which was confirmed by the increased photocurrent intensity of MC0.30, as shown in Fig. 7(a). Therefore, compared with the bare MoS_2 NSs and CdS NWs, as a result of the improved separation of charge carriers and the reduced charge-transfer resistance of the MC0.30 composite, the photoelectrochemical and photocatalytic water reduction by electrons on the catalyst surface was facilitated to a greater degree for MC0.30 (similar for the other MoS_2 NS/CdS NW HRSs). This explains the remarkably boosted activities of these composites with regard to the photocurrent response and photocatalytic H_2 evolution.

3.3 Structural elucidations for enhanced photocatalytic activities

To elucidate the relationship between the structure and performance of the 1D multi-node MoS_2/CdS hetero-NWs, the electronic band structures of the MoS_2 NSs and CdS NWs were investigated. As shown in Figs. 8(a) and 8(b) (as well as Fig. S12 in the ESM), the bandgaps of pure CdS NWs and MoS_2 NSs were determined via Kubelka–Munk methods to be 2.42 eV (direct type) and 1.65 eV (indirect type), respectively. The bandgap of bulk MoS_2 is ~1.3 eV [57]. In this study, the bandgap of the ultrathin MoS_2 NWs increased to 1.65 eV, mainly owing to the quantum size effects [61]. The Mott–Schottky data for the CdS NWs and MoS_2 NSs were obtained with an alternating-current
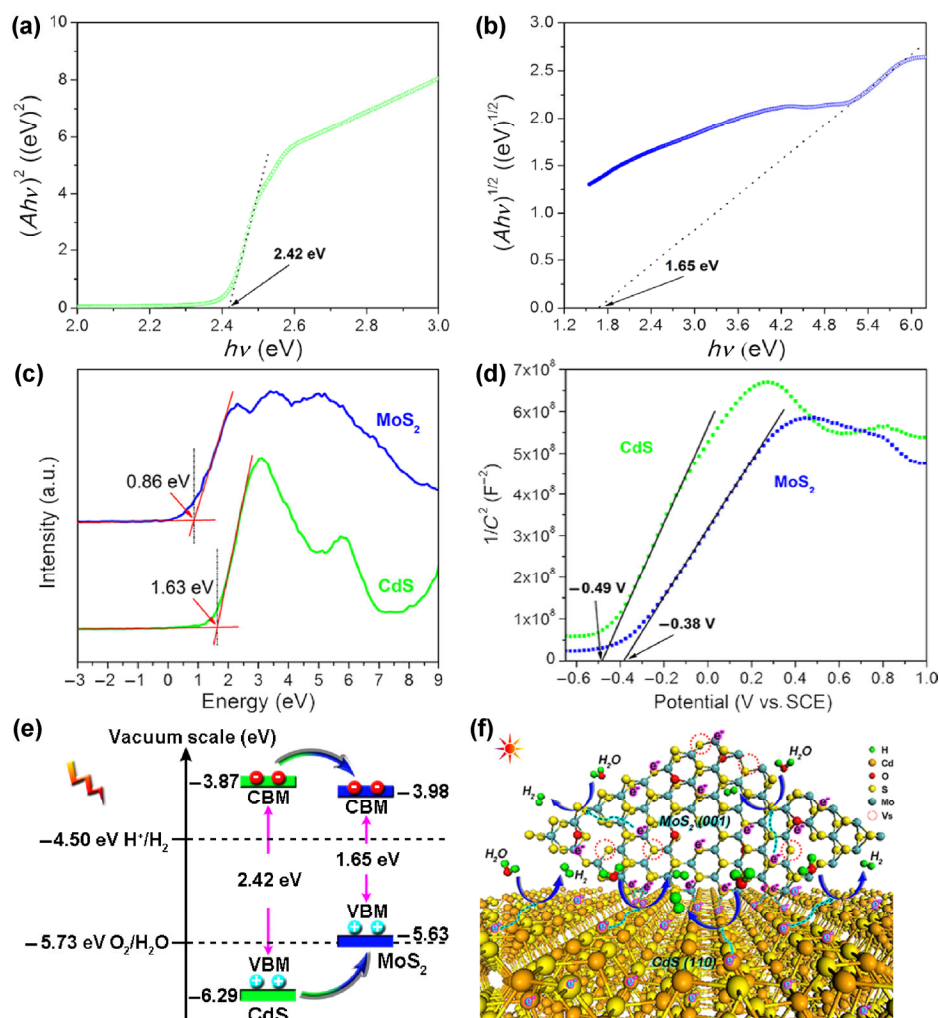
Figure 8 Determination of bandgap energies of (a) CdS NWs and (b) MoS$_2$ NSs. XPS valence-band spectra and Mott–Schottky curves for MoS$_2$ NSs and CdS NWs are shown in (c) and (d), respectively. (e) Energy-band alignments of individual MoS$_2$ NSs and CdS NWs. (f) Schematic of photocatalytic H$_2$ evolution with the MoS$_2$/CdS HRSs.

frequency of 1 kHz in a 0.5 M Na$_2$SO$_4$ aqueous solution (Fig. 8(d)). Both the samples exhibited positive slopes, indicating that the CdS NWs and the MoS$_2$ NSs were n-type semiconductors [62, 63]. The Fermi energy levels of individual CdS NWs and MoS$_2$ NSs were identified by the intercepts of the curves with the horizontal axis [64–66] to be −0.49 and −0.38 V vs. SCE, which were calibrated [67] by the value of 0.653 V (Fig. S13 in the ESM) to 0.163 and 0.273 V, respectively, vs. a reversible hydrogen electrode (RHE) (−4.66 and −4.77 eV, respectively, in vacuum scale). The XPS valence-band spectra shown in Fig. 8(c) indicate that the valence-band maxima (VBM) of the MoS$_2$ NSs and CdS NWs were 0.86 and 1.63 eV lower than their corresponding Fermi levels, respectively. By combining

the Fermi energy levels of the CdS NWs and MoS$_2$ NSs with their bandgap energies and XPS valence-band spectra, the corresponding band structures were established (Fig. 8(e)). According to the constructed energy-band alignments, the Fermi levels for both the CdS NWs (−4.66 eV) and the MoS$_2$ NSs (−4.77 eV) were closer to their respective conduction bands than to the valence bands, which suggests that the synthesized CdS NWs and MoS$_2$ NSs were n-type semiconductors, agreeing well with the analysis of the Mott–Schottky curves. As shown in Fig. 8(e), the position of the conduction-band minimum (CBM) for the CdS NWs was higher than that for the MoS$_2$ NSs, while the VBM for the CdS NWs was lower than that for the MoS$_2$ NSs. Therefore, for the MoS$_2$ NS/CdS NW

HRSs, under irradiation, the photogenerated electrons were transferred spontaneously from the CdS CBM to the MoS$_2$ CBM through the formed junction interfaces. In contrast, the holes remaining in the VBM of CdS were injected into the VBM of MoS$_2$. Consequently, the recombination of photoexcited electrons and holes was significantly slowed by the MoS$_2$/CdS composites, improving their activities for the photoelectrochemical and photocatalytic reactions. In addition, according to the Gibbs free energies of H$_2$ adsorption on the catalyst edges calculated theoretically by Xie J. et al. [27], compared with the pristine MoS$_2$ system, the O-incorporated MoS$_2$ slab exhibited smaller differential binding free energies at different H coverages, revealing that the latter required a lower energy barrier to drive the H$_2$ evolution reaction. Moreover, according to Xie J. et al. [27], the calculated density of states indicated that the bandgap of a pristine 2H-MoS$_2$ slab was narrowed after the incorporation of O. Thus, the O incorporation in the MoS$_2$ ultrathin NSs could have led to additional charge carriers and a higher intrinsic conductivity, facilitating the H$_2$ generation. Consequently, for the MoS$_2$/CdS HRSs, the grown MoS$_2$ ultrathin NSs with O incorporation may have had a lower energy barrier for H$_2$ evolution and a higher electric conductivity compared with the pristine counterpart, enhancing their photoelectrocatalytic capabilities. On the other hand, there were numerous unsaturated S and Cd atoms on the defect-rich {0001} faceted MoS$_2$ NSs and {11$\bar{2}$0} surrounding CdS NWs, which functioned as catalytic active sites to reduce the reaction activation energy and thus improve the reactivities. The 1D well-crystallized CdS stems in the HRSs may have provided a pathway along the longitudinal dimension for the fast transfer and separation of charge carriers, facilitating the catalytic reactions. The photocatalytic H$_2$ formation under visible-light irradiation at the MoS$_2$ {0001}/CdS {11$\bar{2}$0} interface is illustrated in Fig. 8(f).

4 Conclusions

We prepared 1D multi-node MoS$_2$/CdS hetero-NWs with different Mo-to-Cd ratios under hydrothermal conditions for the first time, in which flower-like sheaths were assembled by O-incorporated defect-rich ultrathin {0001} MoS$_2$ NSs and CdS NWs were surrounded by {11$\bar{2}$0} facets parallel to the *c*-axis. The MoS$_2$ NS/CdS NW hybrids demonstrated excellent visible-light photocatalytic activity for H$_2$ evolution from water splitting compared with Pt/CdS NWs, individual MoS$_2$ NSs and CdS NWs, and their physical mixtures. The enhanced photocatalytic capability of the MoS$_2$/CdS composites is attributed to the abundant active sites of MoS$_2$ NSs and CdS NWs, the intimate heterojunctions formed between the MoS$_2$ and CdS, and the well-defined 1D nano-architecture. Our findings may inspire the development of methods for the engineering and construction of novel nano-structures for advanced applications.

Electronic Supplementary Material: Supplementary material (UV–vis absorption spectra, BET surface areas, ICP data, EPR spectrum, TGA-DTA analyse, N$_2$ adsorption isotherms and pore-size distribution, additional XRD, TEM, and XPS results, and time-resolved H$_2$ evolution curves of synthesized MoS$_2$/CdS heterostructures; calibration of SCE to RHE; atomic structural models of CdS {01$\bar{1}$0} and {0001} planes; and comparison of the H$_2$ formation activities of MoS$_2$/CdS hybrids reported previously) is available in the online version of this article at http://dx.doi.org/10.1007/s12274-017-1497-3.

References

[1] Chang, K.; Hai, X.; Ye, J. H. Transition metal disulfides as noble-metal-alternative co-catalysts for solar hydrogen production. *Adv. Energy Mater.* **2016**, *6*, 1502555.

[2] Fujishima, A.; Honda, K. Electrochemical photolysis of water at a semiconductor electrode. *Nature* **1972**, *238*, 37–38.

[3] Peng, T. Y.; Li, K.; Zeng, P.; Zhang, Q. G.; Zhang, X. G. Enhanced photocatalytic hydrogen production over graphene

oxide–cadmium sulfide nanocomposite under visible light irradiation. *J. Phys. Chem. C* **2012**, *116*, 22720–22726.

[4]   Chen, J. Z.; Wu, X. J.; Yin, L. S.; Li, B.; Hong, X.; Fan, Z. X.; Chen, B.; Xue, C.; Zhang, H. One-pot synthesis of CdS nanocrystals hybridized with single-layer transition-metal dichalcogenide nanosheets for efficient photocatalytic hydrogen evolution. *Angew. Chem., Int. Ed.* **2015**, *54*, 1210–1214.

[5]   Marschall, R. Semiconductor composites: Strategies for enhancing charge carrier separation to improve photocatalytic activity. *Adv. Funct. Mater.* **2014**, *24*, 2421–2440.

[6]   Lu, X.; Luo, X.; Zhang, J.; Quek, S. Y.; Xiong, Q. H. Lattice vibrations and Raman scattering in two-dimensional layered materials beyond graphene. *Nano Res.* **2016**, *9*, 3559–3597.

[7]   Ma, X. Y.; Li, J. Q.; An, C. H.; Feng, J.; Chi, Y. H.; Liu, J. X.; Zhang, J.; Sun, Y. G. Ultrathin Co(Ni)-doped MoS_2 nanosheets as catalytic promoters enabling efficient solar hydrogen production. *Nano Res.* **2016**, *9*, 2284–2293.

[8]   Bai, S.; Wang, L. M.; Chen, X. Y.; Du, J. T.; Xiong, Y. J. Chemically exfoliated metallic MoS_2 nanosheets: A promising supporting co-catalyst for enhancing the photocatalytic performance of TiO_2 nanocrystals. *Nano Res.* **2015**, *8*, 175–183.

[9]   Simon, T.; Bouchonville, N.; Berr, M. J.; Vaneski, A.; Adrović, A.; Volbers, D.; Wyrwich, R.; Döblinger, M.; Susha, A. S.; Rogach, A. L. et al. Redox shuttle mechanism enhances photocatalytic H_2 generation on Ni-decorated CdS nanorods. *Nat. Mater.* **2014**, *13*, 1013–1018.

[10] Du, Y. P.; Chen, B.; Yin, Z. Y.; Liu, Z. Q.; Zhang, H. Phosphine-free, low-temperature synthesis of tetrapod-shaped CdS and its hybrid with Au nanoparticles. *Small* **2014**, *10*, 4727–4734.

[11] Zhou, K. B.; Wang, X.; Sun, X. M.; Peng, Q.; Li, Y. D. Enhanced catalytic activity of ceria nanorods from well-defined reactive crystal planes. *J. Catal.* **2005**, *229*, 206–212.

[12] Chen, W.; Kuang, Q.; Xie, Z. X. Morphology evolution of $NaTaO_3$ submicrometer single-crystals: From cubes to quasi-spheres. *Sci. China Mater.* **2015**, *58*, 281–288.

[13] Lai, X.-Y.; Wang, C.-R.; Jin, Q.; Yu, R.-B.; Wang, D. Synthesis and photocatalytic activity of hierarchical flower-like $SrTiO_3$ nanostructure. *Sci. China Mater.* **2015**, *58*, 192–197.

[14] Kuang, Q.; Wang, X.; Jiang, Z. Y.; Xie, Z. X.; Zheng, L. S. High-energy-surface engineered metal oxide micro- and nanocrystallites and their applications. *Acc. Chem. Res.* **2014**, *47*, 308–318.

[15] Jiang, Q. N.; Jiang, Z. Y.; Zhang, L.; Lin, H. X.; Yang, N.; Li, H.; Liu, D. Y.; Xie, Z. X.; Tian, Z. Q. Synthesis and high electrocatalytic performance of hexagram shaped gold particles having an open surface structure with kinks. *Nano*

[16] Jin, M. S.; Liu, H. Y.; Zhang, H.; Xie, Z. X.; Liu, J. Y.; Xia, Y. N. Synthesis of Pd nanocrystals enclosed by {100} facets and with sizes <10 nm for application in CO oxidation. *Nano Res.* **2011**, *4*, 83–91.

[17] Zhang, Z. C.; Liu, Y.; Chen, B.; Gong, Y.; Gu, L.; Fan, Z. X.; Yang, N. L.; Lai, Z. C.; Chen, Y.; Wang, J. et al. Submonolayered Ru deposited on ultrathin Pd nanosheets used for enhanced catalytic applications. *Adv. Mater.* **2016**, *28*, 10282–10286.

[18] Zhang, Z. C.; Luo, Z. M.; Chen, B.; Wei, C.; Zhao, J.; Chen, J. Z.; Zhang, X.; Lai, Z. C.; Fan, Z. X.; Tan, C. L. et al. One-pot synthesis of highly anisotropic five-fold-twinned PtCu nanoframes used as a bifunctional electrocatalyst for oxygen reduction and methanol oxidation. *Adv. Mater.* **2016**, *28*, 8712–8717.

[19] Fan, Z. X.; Luo, Z. M.; Huang, X.; Li, B.; Chen, Y.; Wang, J.; Hu, Y. L.; Zhang, H. Synthesis of 4h/fcc noble multimetallic nanoribbons for electrocatalytic hydrogen evolution reaction. *J. Am. Chem. Soc.* **2016**, *138*, 1414–1419.

[20] Yang, S. Y.; Shim, G. W.; Seo, S.-B.; Choi, S.-Y. Effective shape-controlled growth of monolayer MoS_2 flakes by powder-based chemical vapor deposition. *Nano Res.* **2017**, *10*, 255–262.

[21] Karunadasa, H. I.; Montalvo, E.; Sun, Y.; Majda, M.; Long, J. R.; Chang, C. J. A molecular MoS_2 edge site mimic for catalytic hydrogen generation. *Science* **2012**, *335*, 698–702.

[22] Wang, H. T.; Tsai, C.; Kong, D. S.; Chan, K. R.; Abild-Pedersen, F.; Nørskov, J. K.; Cui, Y. Transition-metal doped edge sites in vertically aligned MoS_2 catalysts for enhanced hydrogen evolution. *Nano Res.* **2015**, *8*, 566–575.

[23] Liu, D. B.; Xu, W. Y.; Liu, Q.; He, Q.; Haleem, Y. A.; Wang, C. D.; Xiang, T.; Zou, C. W.; Chu, W. S.; Zhong, J. et al. Unsaturated-sulfur-rich MoS_2 nanosheets decorated on free-standing SWNT film: Synthesis, characterization and electrocatalytic application. *Nano Res.* **2016**, *9*, 2079–2087.

[24] Zong, X.; Yan, H. J.; Wu, G. P.; Ma, G. J.; Wen, F. Y.; Wang, L.; Li, C. Enhancement of photocatalytic H_2 evolution on CdS by loading MoS_2 as cocatalyst under visible light irradiation. *J. Am. Chem. Soc.* **2008**, *130*, 7176–7177.

[25] Chang, K.; Mei, Z. W.; Wang, T.; Kang, Q.; Ouyang, S. X.; Ye, J. H. MoS_2/graphene cocatalyst for efficient photocatalytic H_2 evolution under visible light irradiation. *ACS Nano* **2014**, *8*, 7078–7087.

[26] Wu, N. Q.; Wang, J.; Tafen de, N.; Wang, H.; Zheng, J. G.; Lewis, J. P.; Liu, X. G.; Leonard, S. S.; Manivannan, A. Shape-enhanced photocatalytic activity of single-crystalline anatase TiO_2 (101) nanobelts. *J. Am. Chem. Soc.* **2010**, *132*, 6679–6685.

[27] Xie, J. F.; Zhang, J. J.; Li, S.; Grote, F.; Zhang, X. D.; Zhang, H.; Wang, R. X.; Lei, Y.; Pan, B. C.; Xie, Y. Controllable disorder engineering in oxygen-incorporated MoS_2 ultrathin nanosheets for efficient hydrogen evolution. *J. Am. Chem. Soc.* **2013**, *135*, 17881–17888.

[28] Zhou, W. J.; Yin, Z. Y.; Du, Y. P.; Huang, X.; Zeng, Z. Y.; Fan, Z. X.; Liu, H.; Wang, J. Y.; Zhang, H. Synthesis of few-layer MoS_2 nanosheet-coated TiO_2 nanobelt heterostructures for enhanced photocatalytic activities. *Small* **2013**, *9*, 140–147.

[29] He, J.; Chen, L.; Wang, F.; Liu, Y.; Chen, P.; Au, C. T.; Yin, S. F. CdS nanowires decorated with ultrathin MoS_2 nanosheets as an efficient photocatalyst for hydrogen evolution. *ChemSusChem* **2016**, *9*, 624–630.

[30] Xing, X. N.; Zhang, Q.; Huang, Z.; Lu, Z. J.; Zhang, J. B.; Li, H. Q.; Zeng, H. B.; Zhai, T. Y. Strain driven spectral broadening of Pb ion exchanged CdS nanowires. *Small* **2016**, *12*, 874–881.

[31] Cao, B. L.; Jiang, Y.; Wang, C.; Wang, W. H.; Wang, L. Z.; Niu, M.; Zhang, W. J.; Li, Y. Q.; Lee, S. T. Synthesis and lasing properties of highly ordered CdS nanowire arrays. *Adv. Funct. Mater.* **2007**, *17*, 1501–1506.

[32] Li, H.; Zhang, Q.; Yap, C. C. R.; Tay, B. K.; Edwin, T. H. T.; Olivier, A.; Baillargeat, D. From bulk to monolayer MoS_2: Evolution of Raman scattering. *Adv. Funct. Mater.* **2012**, *22*, 1385–1390.

[33] Xie, J. F.; Zhang, H.; Li, S.; Wang, R. X.; Sun, X.; Zhou, M.; Zhou, J. F.; Lou, X. W.; Xie, Y. Defect-rich MoS_2 ultrathin nanosheets with additional active edge sites for enhanced electrocatalytic hydrogen evolution. *Adv. Mater.* **2013**, *25*, 5807–5813.

[34] Seguin, L.; Figlarz, M.; Cavagnat, R.; Lassègues, J. C. Infrared and Raman spectra of MoO_3 molybdenum trioxides and $MoO_3 \cdot x H_2O$ molybdenum trioxide hydrates. *Spectrochim. Acta Part A: Molecul. Biomol. Spectr.* **1995**, *51*, 1323–1344.

[35] Weng, B.; Zhang, X.; Zhang, N.; Tang, Z.-R.; Xu, Y.-J. Two-dimensional MoS_2 nanosheet-coated Bi_2S_3 discoids: Synthesis, formation mechanism, and photocatalytic application. *Langmuir* **2015**, *31*, 4314–4322.

[36] Splendiani, A.; Sun, L.; Zhang, Y. B.; Li, T. S.; Kim, J.; Chim, C. Y.; Galli, G.; Wang, F. Emerging photoluminescence in monolayer MoS_2. *Nano Lett.* **2010**, *10*, 1271–1275.

[37] Cai, L.; He, J. F.; Liu, Q. H.; Yao, T.; Chen, L.; Yan, W. S.; Hu, F. C.; Jiang, Y.; Zhao, Y. D.; Hu, T. D. et al. Vacancy-induced ferromagnetism of MoS_2 nanosheets. *J. Am. Chem. Soc.* **2015**, *137*, 2622–2627.

[38] Li, G. S.; Boerio-Goates, J.; Woodfield, B. F.; Li, L. P. Evidence of linear lattice expansion and covalency enhancement in rutile TiO_2 nanocrystals. *Appl. Phys. Lett.* **2004**, *85*, 2059–2061.

[39] Ayyub, P.; Palkar, V. R.; Chattopadhyay, S.; Multani, M. Effect of crystal size reduction on lattice symmetry and cooperative properties. *Phys. Rev. B* **1995**, *51*, 6135–6138.

[40] Li, X. D.; Li, W.; Li, M. C.; Cui, P.; Chen, D. H.; Gengenbach, T.; Chu, L. H.; Liu, H. Y.; Song, G. S. Glucose-assisted synthesis of the hierarchical TiO_2 nanowire@MoS_2 nanosheet nanocomposite and its synergistic lithium storage performance. *J. Mater. Chem. A* **2015**, *3*, 2762–2769.

[41] Buonsanti, R.; Grillo, V.; Carlino, E.; Giannini, C.; Kipp, T.; Cingolani, R.; Cozzoli, P. D. Nonhydrolytic synthesis of high-quality anisotropically shaped brookite TiO_2 nanocrystals. *J. Am. Chem. Soc.* **2008**, *130*, 11223–11233.

[42] Cozzoli, P. D.; Pellegrino, T.; Manna, L. Synthesis, properties and perspectives of hybrid nanocrystal structures. *Chem. Soc. Rev.* **2006**, *35*, 1195–1208.

[43] Cheng, H. M.; Ma, J. M.; Zhao, Z. G.; Qi, L. M. Hydrothermal preparation of uniform nanosize rutile and anatase particles. *Chem. Mater.* **1995**, *7*, 663–671.

[44] Sau, T. K.; Rogach, A. L. Nonspherical noble metal nanoparticles: Colloid-chemical synthesis and morphology control. *Adv. Mater.* **2010**, *22*, 1781–1804.

[45] Kibsgaard, J.; Chen, Z. B.; Reinecke, B. N.; Jaramillo, T. F. Engineering the surface structure of MoS_2 to preferentially expose active edge sites for electrocatalysis. *Nat. Mater.* **2012**, *11*, 963–969.

[46] Yang, Y.; Fei, H. L.; Ruan, G. D.; Xiang, C. S.; Tour, J. M. Edge-oriented MoS_2 nanoporous films as flexible electrodes for hydrogen evolution reactions and supercapacitor devices. *Adv. Mater.* **2014**, *26*, 8163–8168.

[47] Chang, Y.-H.; Nikam, R. D.; Lin, C.-T.; Huang, J.-K.; Tseng, C.-C.; Hsu, C.-L.; Cheng, C.-C.; Su, C.-Y.; Li, L.-J.; Chua, D. H. C. Enhanced electrocatalytic activity of MoS_x on TCNQ-treated electrode for hydrogen evolution reaction. *ACS Appl. Mater. Interfaces* **2014**, *6*, 17679–17685.

[48] Xiong, J. H.; Liu, Y. H.; Wang, D. K.; Liang, S. J.; Wu, W. M.; Wu, L. An efficient cocatalyst of defect-decorated MoS_2 ultrathin nanoplates for the promotion of photocatalytic hydrogen evolution over CdS nanocrystal. *J. Mater. Chem. A* **2015**, *3*, 12631–12635.

[49] Louis, C.; Che, M. EPR investigation of the coordination sphere of molybdenum(5+) ions on thermally reduced silica-supported molybdenum catalysts prepared by the grafting method. *J. Phys. Chem.* **1987**, *91*, 2875–2883.

[50] Blinc, R.; Cevc, P.; Mrzel, A.; Arčon, D.; Remškar, M.; Milia, F.; Laguta, V. V. EPR spectra of MoS_2/C_{60}. *Phys. Status Solidi (B)* **2010**, *247*, 3033–3034.

[51] Majeed, I.; Nadeem, M. A.; Al-Oufi, M.; Nadeem, M. A.; Waterhouse, G. I. N.; Badshah, A.; Metson, J. B.; Idriss, H. On the role of metal particle size and surface coverage for

photo-catalytic hydrogen production: A case study of the Au/CdS system. *Appl. Catal. B: Environ.* **2016**, *182*, 266–276.

[52] Gao, P.; Liu, J.; Sun, D. D.; Ng, W. Graphene oxide–CdS composite with high photocatalytic degradation and disinfection activities under visible light irradiation. *J. Hazard. Mater.* **2013**, *250–251*, 412–420.

[53] Sun, Y. M.; Hu, X. L.; Luo, W.; Huang, Y. H. Self-assembled hierarchical MoO_2/graphene nanoarchitectures and their application as a high-performance anode material for lithium-ion batteries. *ACS Nano* **2011**, *5*, 7100–7107.

[54] Merki, D.; Fierro, S.; Vrubel, H.; Hu, X. L. Amorphous molybdenum sulfide films as catalysts for electrochemical hydrogen production in water. *Chem. Sci.* **2011**, *2*, 1262–1267.

[55] Zhang, J.; Zhu, Z. P.; Feng, X. L. Construction of two-dimensional MoS_2/CdS p–n nanohybrids for highly efficient photocatalytic hydrogen evolution. *Chem.—Eur. J.* **2014**, *20*, 10632–10635.

[56] Zhuang, T. T.; Liu, Y.; Sun, M.; Jiang, S. L.; Zhang, M. W.; Wang, X. C.; Zhang, Q.; Jiang, J.; Yu, S. H. A unique ternary semiconductor-(semiconductor/metal) nano-architecture for efficient photocatalytic hydrogen evolution. *Angew. Chem., Int. Ed.* **2015**, *127*, 11657–11662.

[57] Mak, K. F.; Lee, C.; Hone, J.; Shan, J.; Heinz, T. F. Atomically thin MoS_2: A new direct-gap semiconductor. *Phys. Rev. Lett.* **2010**, *105*, 136805.

[58] Bell, N. J.; Ng, Y. H.; Du, A. J.; Coster, H.; Smith, S. C.; Amal, R. Understanding the enhancement in photoelectro-chemical properties of photocatalytically prepared TiO_2-reduced graphene oxide composite. *J. Phys. Chem. C* **2011**, *115*, 6004–6009.

[59] Wu, T.; Zhang, Q.; Hou, Y.; Wang, L.; Mao, C. Y.; Zheng, S.-T.; Bu, X. H.; Feng, P. Y. Monocopper doping in Cd-In-S supertetrahedral nanocluster via two-step strategy and enhanced photoelectric response. *J. Am. Chem. Soc.* **2013**, *135*, 10250–10253.

[60] Kim, E. S.; Nishimura, N.; Magesh, G.; Kim, J. Y.; Jang, J. W.; Jun, H.; Kubota, J.; Domen, K.; Lee, J. S. Fabrication of $CaFe_2O_4$/TaON heterojunction photoanode for photoelectro-chemical water oxidation. *J. Am. Chem. Soc.* **2013**, *135*, 5375–5383.

[61] Thurston, T. R.; Wilcoxon, J. P. Photooxidation of organic chemicals catalyzed by nanoscale MoS_2. *J. Phys. Chem. B* **1999**, *103*, 11–17.

[62] Meng, F. K.; Li, J. T.; Cushing, S. K.; Zhi, M. J.; Wu, N. Q. Solar hydrogen generation by nanoscale p–n junction of p-type molybdenum disulfide/n-type nitrogen-doped reduced graphene oxide. *J. Am. Chem. Soc.* **2013**, *135*, 10286–10289.

[63] Wang, G. M.; Ling, Y. C.; Wheeler, D. A.; George, K. E. N.; Horsley, K.; Heske, C.; Zhang, J. Z.; Li, Y. Facile synthesis of highly photoactive α-Fe_2O_3-based films for water oxidation. *Nano Lett.* **2011**, *11*, 3503–3509.

[64] Xu, B.; He, P. L.; Liu, H. L.; Wang, P. P.; Zhou, G.; Wang, X. A 1D/2D helical CdS/$ZnIn_2S_4$ nano-heterostructure. *Angew. Chem., Int. Ed.* **2014**, *53*, 2339–2343.

[65] Bai, Y.; Ye, L. Q.; Wang, L.; Shi, X.; Wang, P. Q.; Bai, W.; Wong, P. K. g-C_3N_4/$Bi_4O_5I_2$ heterojunction with I_3^-/I^- redox mediator for enhanced photocatalytic CO_2 conversion. *Appl. Catal. B: Environ.* **2016**, *194*, 98–104.

[66] Li, H. F.; Yu, H. T.; Quan, X.; Chen, S.; Zhang, Y. B. Uncovering the key role of the Fermi level of the electron mediator in a Z-scheme photocatalyst by detecting the charge transfer process of WO_3-metal-gC_3N_4 (metal = Cu, Ag, Au). *ACS Appl. Mater. Interfaces* **2016**, *8*, 2111–2119.

[67] Li, Y. G.; Zhou, W.; Wang, H. L.; Xie, L. M.; Liang, Y. Y.; Wei, F.; Idrobo, J. C.; Pennycook, S. J.; Dai, H. J. An oxygen reduction electrocatalyst based on carbon nanotube-graphene complexes. *Nat. Nanotechnol.* **2012**, *7*, 394–400.